



# Similar Fermi-GBM sGRBs to GW/sGRB 170817A in MeV-GeV energies

Sanjeeva Rao Prattipati,<sup>1</sup>  <sup>\*</sup> Reetanjali Moharana<sup>1</sup>  <sup>†</sup> and Sourav Dutta

<sup>1</sup>Department of Physics, Indian Institute of Technology Jodhpur, Jodhpur-342037, India.

Accepted XXX. Received YYY; in original form ZZZ

## ABSTRACT

The rate of observed gravitational waves (GWs) from neutron star-neutron star (NS-NS) mergers detected by the Laser Interferometer Gravitational-Wave Observatory (LIGO) indicates the existence of more than one short gamma-ray bursts (sGRBs) similar to GW/sGRB 170817A within the total gamma-ray bursts (GRBs) recorded by satellite detectors such as BATSE, Fermi-Gamma-ray Burst Monitor (Fermi-GBM), and Swift-Burst Alert Telescope (Swift-BAT). We investigated sGRBs in the Fermi-GBM dataset based on their MeV-GeV  $\gamma$ -ray emission features, to identify sGRBs similar to sGRB 170817A. Any addition of such events can impact the rate of NS-NS CBC events observed by LIGO. SGRB 170817A exhibits two distinct emission components: a non-thermal peak and a thermal component. We adopted a multifaceted approach to identify analogous sGRBs, which involved computing the hardness ratios  $HR_1$  and  $HR_2$  and then clustering them via the K-means algorithm. Our further studies reveal the presence of eight such events in Fermi-GBM data, which will enable us to calculate the rate of electromagnetic (EM) counterparts associated with LIGO GW events (GW+sGRB events) across all observing runs. Giving an estimation, by the end of the  $O_4$  LIGO run, there could be nearly 5 GW+sGRB events. Deviation from this number may raise concerns about our understanding of the evolution of such events over distance.

**Key words:** Gamma rays: bursts, detectors: Fermi-GBM Methods: Hardness Ratio, K-means algorithm.

## 1 INTRODUCTION

The Advanced LIGO and Virgo gravitational wave (GW) radiation observatories detected the only confirmed binary neutron star (BNS) merger on August 17, 2017, through multi-wavelength observations. The event was subsequently identified as sGRB 170817A, which triggered 1.7 seconds after the GW event. The MeV-GeV emissions observed by Fermi-GBM report the event with  $T_{90}^1 = 2.048$  sec (Goldstein et al. 2017). The microminor/kilonovae observed around the event in optical, UV, and IR as a counterpart by SSS17a (Coulter et al. 2017; Villar et al. 2017; Drout et al. 2017; Evans et al. 2017; Tanvir et al. 2017; Smartt et al. 2017; Pian et al. 2017) confirms the presence of heavy elements originated by the r-process of the NS-NS merger. This multimessenger observation confirmed the long-standing theory that one of the origins of sGRBs is the merger of compact objects, such as neutron stars (Poggiani et al. 2020; Eichler et al. 1989; Narayan et al. 1992). Previously, a pulsar survey on NS-NS objects estimation in the near sky (both Galactic and Extragalactic) predicted a reasonable number of BNS events to be observed by LIGO (Kalogera et al. 2001), where the original idea is given in (Narayan et al. 1991; Kalogera et al. 2004). Reference (Kalogera et al. 2001) predicted the NS-NS inspiral detection rates with the then proposed LIGO II, a rate of 2-1300  $\text{yr}^{-1}$  within a distance of 350 Mpc, comparable to the upcoming  $O_5$  run of LIGO. Theoretically, the other way to estimate the rate of NS-NS mergers is through

population synthesis (Belczynski et al. 2007). A phenomenological approach based on the rate of sGRBs observed by Swift, with the well-known redshift (Coward et al. 2012), leads to predictions of lower and upper detection rate limits of (1-180)  $\text{yr}^{-1}$  by Advanced LIGO (aLIGO). The rate density of sGRBs used for this calculation is  $8_{-3}^{+5} - 1100_{-470}^{+700} \text{ Gpc}^{-3} \text{ yr}^{-1}$ .

Interestingly, later observations with Very Long Baseline Interferometry (VLBI) of the sGRB 170817A revealed a super-luminal motion of the later radio afterglow image (Mooley et al. 2018). These observations imply that a powerful relativistic jet broke out from the ejecta making an angle of  $20 \pm 5$  degrees off to us. The observation suggests a jet opening angle  $\theta_j \leq 5$  deg and a difference with the viewing angle of  $(\theta_{obs} - \theta_j) \sim 0.2 - 0.35$  rad. Prior to this event, the existence of a GRB originating from such a highly off-axis jet was uncertain. Although models suggest sGRB viewing angles can range from  $18^\circ$  to  $33^\circ$  (Granot et al. 2018; Howell et al. 2019), this implies that systems with inclinations above  $33^\circ$  or below  $147^\circ$  may not produce observable GRB emission. Additionally, the work in (Mazwi et al. 2024) using BNS events from LIGO (GW170817 and GW190425), Neutron star-Black hole (NS-BH) (GW190917\_114630 and GW200115\_042309), and GW190425 suggests that the reason for the further absence of compact binary coalescence (CBC) with MeV-GeV emissions is due to the large inclinations. Hence, a detailed study on the visibility of sGRBs at off-axis angles, both theoretically and through significant observations, can also impact the study of CBC GW rates with EM counterparts.

According to further relevant works where only the LIGO detected BNS mergers events have been considered, the event rate of GW events with EM counterparts is calculated as (GW/sGRBs

<sup>\*</sup> E-mail: p23ph0011@iitj.ac.in

<sup>†</sup> reetanjali@iitj.ac.in

<sup>1</sup>  $T_{90}$  is the duration in which the central 90% of the gamma-ray signal is detected.

170817A),  $R = 1540^{+3200}_{-1220} \text{ Gpc}^{-3} \text{ yr}^{-1}$  (Abbott et al. 2017, 2023a). While recent findings, utilizing updated LIGO sensitivity and detection volume, yield a new rate estimated as  $680 - 1300 \text{ Gpc}^{-3} \text{ yr}^{-1}$  (Hayes et al. 2023). This rate implies that BNS mergers are rather frequent and play a significant role in the universe's r-process nucleosynthesis. Additional detections with the ongoing GW detectors network, including LIGO, Virgo, and the Japanese Kamioka Gravitational Wave Detector (KAGRA), along with the upcoming LIGO India (Pandey et al. 2025), aim to provide a precise measurement of the rate estimate of BNS events by looking deeper into the sky. In the meantime, an estimation of the rate by examining the sGRB behaviors of such events can provide a better understanding to tune the observations. Hence, a detailed statistical interpretation is necessary to identify similar sGRBs to sGRB 170817A among the previously observed sGRBs by the three gamma-ray satellite detectors: BATSE, Fermi-GBM, and Swift. A similar attempt has been made by several groups, including the Fermi-GBM collaboration (von Kienlin et al. 2019) and the Swift team, which detected sGRBs (Kapadia et al. 2024). In this work, we present a statistically detailed study of the Fermi-GBM sGRBs, complementing and adding new results to the aforementioned studies.

The peculiarity of the sGRB 170817A follows the presence of two distinct emission components over the  $T_{90}$  of 2.048 sec. The first emission from -0.192 sec to 1.216 sec is a soft pulse with alpha ( $\alpha$ ) =  $0.85 \pm 1.38$  and peak emission  $E_{\text{peak}} = 215 \pm 54 \text{ keV}$ , and the second emission, within 1.216 sec to 1.856 sec follows a softer thermal tail at the energy  $kT = 10.3 \pm 1.5 \text{ keV}$  (Goldstein et al. 2017; von Kienlin et al. 2019). This peculiar feature is explained as being observed with an off-axis viewing angle of the jet (Troja et al. 2017; Margutti et al. 2017; Fong et al. 2017; Margalit & Metzger 2017). Our investigation focuses on identifying and characterizing dual-peak structures similar to those observed in other sGRB light curves, with an emphasis on distinguishing between thermal and nonthermal features. Although clearly the unique feature of the sGRB is its low luminosity,  $L_{\text{iso}} = 1.6 \times 10^{47} \text{ erg s}^{-1}$  (Zhang et al. 2018). Unfortunately, without knowing the distances of each sGRB, we cannot make this a search criterion.

The structure of the paper is as follows: Section 2 explains the calculation of the expected number of sGRBs for all major satellite detectors up to 17 August 2017, following the LIGO observed rate for BNS. Section 3 describes the selection of the sGRB events from the Fermi-GBM catalog for their  $HR_1$  and  $HR_2$  calculation. The detailed tools used for analysis are explained in section 4. In subsection 4.1 we discuss the machine learning (ML) model K-means clustering for the classification of sGRBs, and further in subsection 4.2 we discuss the light curve and spectral analysis. Finally, in section 5 and section 6, we present the obtained results, a summary, and the future scope of this work.

## 2 EXPECTED sGRB RATE

The EM counterpart of a GW event was observed and identified as the short GRB 170817A, which originated from an NS-NS merger, during the second Observing run ( $O_2$ ) of Advanced LIGO. The running time of the  $O_2$  run is from November 30, 2016, to August 25, 2017. Remarkably, the rate of such an observation recorded as  $R = 1540^{+3200}_{-1220} \text{ Gpc}^{-3} \text{ yr}^{-1}$  (Abbott et al. 2017), which was quite high compared to the expected rate of NS-NS merger from theoretical estimations. A detailed further analysis and interpretation predict the rate of such events with LIGO to be  $R_{\text{GW}} = 680 - 1300 \text{ Gpc}^{-3} \text{ yr}^{-1}$  (Hayes et al. 2023). Considering both these rates of sGRBs, we can

calculate the total number of such events that must have been listed in the major satellite detectors.

$$N_{\text{obs}} = R_{\text{GW}} V_x \mathbb{T} \mathbb{D} \left( \frac{\Delta\Omega_x}{4\pi} \right). \quad (1)$$

$r_x$  is the distance till which a sGRB mimicking sGRB170817A is significantly above the background. Reference (Zhang et al. 2018) showed that the first peak would be visible if the GRB is at a distance of a maximum of 65 Mpc, whereas the second peak would merge with the background at a distance of 55 Mpc. Hence we have taken  $r_x = 65 \text{ Mpc}$  and 55 Mpc, and the corresponding volume,  $V_x = \left(\frac{4}{3}\right) \pi r_x^3$ .  $\mathbb{D}$  is the duty cycle of the detector, and  $\mathbb{T}$  is the corresponding detectors total operating time. The values of these parameters for the major detectors, Fermi-GBM, BATSE, and Swift, are listed in Table 1. The details of the expected sGRBs within the detector data are also listed in Table 1. It is worth noting that, based on the Fermi-GBM data, a total of 5.06 sGRBs are expected to originate from BNS systems at a distance of 65 Mpc, assuming a rate of  $1300 \text{ Gpc}^{-3} \text{ yr}^{-1}$ . Note that the total number calculation excludes the estimation of the off-axis angle, which may further reduce the estimated number.

## 3 METHODOLOGY FOR SELECTION OF sGRB EVENTS

For simplicity and clarity, we restrict our analysis to only one detector, Fermi-GBM, for our subsequent statistical studies. In a future study, we would expand the same analysis, including all the three major detectors, BATSE, Swift, and Fermi-GBM, where we will have to consider calibration between the detectors. After the launch of the Gamma-ray Large Area Space Telescope (GLAST), Fermi-GBM began detecting GRBs on July 17, 2008. To date, it has observed more than 4091 GRBs<sup>2</sup> with a rate of nearly one GRB per day. The detector covers almost the full sky in one orbit.

We collected the sGRBs from the Fermi-GBM catalog (Bhat et al. 2016) available on the NASA HEASARC website. Subsequently following steps are adopted to form the sample twining of sGRB 170817A.

(i) All GRBs within  $T_{90} < 2.05$  sec before the date of sGRB 170817A have been selected to initiate the analysis. This formed a sample of 635 sGRBs.

(ii) The significant emission of sGRB 170817A was at the first peak  $T_0 - 0.192$  sec to  $T_0 + 0.064$  sec, where  $T_0$  is the starting time of the GRB. The spectral form for this period followed by a Comptonized model (Comp) function (Gruber et al. 2014) with three parameters, amplitude ( $A$ ) in  $\text{photon s}^{-1} \text{ cm}^{-2} \text{ keV}^{-1}$ , spectral index ( $\alpha$ ), and peak energy ( $E_{\text{peak}}$ ) in keV, and  $\epsilon_{\gamma, \text{piv}}$  is always kept at 100 keV for all the cases (Poolakkil et al. 2021).

$$F_{\text{Comp}}(\epsilon_\gamma) = A \left( \frac{\epsilon_\gamma}{\epsilon_{\gamma, \text{piv}}} \right)^\alpha \exp \left[ -\frac{(\alpha + 2)\epsilon_\gamma}{E_{\text{peak}}} \right] \quad (2)$$

$$F_{\text{PL}}(\epsilon_\gamma) = A \left( \frac{\epsilon_\gamma}{\epsilon_{\gamma, \text{piv}}} \right)^\alpha \quad (3)$$

sGRB 170817A has  $E_{\text{peak}}$  and  $\alpha$  value that represent a softer emission and consist of a smaller set in the catalog (Zhang et al. 2018)). Hence, out of the 635 sGRBs we selected the sGRBs below the upper limit of the  $1\sigma$  value of  $E_{\text{peak}}$ , which is 317 keV. This now forms a set of 80 sGRBs. We have shown this process and cut-off values of  $E_{\text{peak}}$  and  $\alpha$  in Figure 1.

<sup>2</sup> <https://heasarc.gsfc.nasa.gov/W3Browse/fermi/fermigbrst.html>

**Table 1.** Number of events for different detectors following the LIGO rate for NS-NS mergers. \* denotes that the partial sky coverage of BATSE is included in its effective duty cycle,  $\mathbb{D}$  is taken from these ref, for Fermi-GBM :(Meegan et al. 1998), BATSE & Swift:(Porciani & Madau 2001)

Detectors	T	$\Delta\Omega$ [sr]	$\mathbb{D}$	Number of events					
				65 Mpc	55 Mpc	65 Mpc		55 Mpc	
				1540 Gpc <sup>-3</sup> yr <sup>-1</sup>	1540 Gpc <sup>-3</sup> yr <sup>-1</sup>	1300 Gpc <sup>-3</sup> yr <sup>-1</sup>	680 Gpc <sup>-3</sup> yr <sup>-1</sup>	1300 Gpc <sup>-3</sup> yr <sup>-1</sup>	680 Gpc <sup>-3</sup> yr <sup>-1</sup>
Fermi-GBM	17 Jul, 2008 - 17 Aug, 2017	9.5	0.5	6.08	3.68	5.06	2.65	3.07	1.60
BATSE	21 Apr, 1991 - 17 Aug, 2000	4 $\pi$ *	0.456	7.54	4.57	6.28	3.28	3.80	1.99
Swift	17 Dec, 2004 - 17 Aug, 2017	1.4	0.78	1.95	1.18	1.62	0.84	0.98	0.51

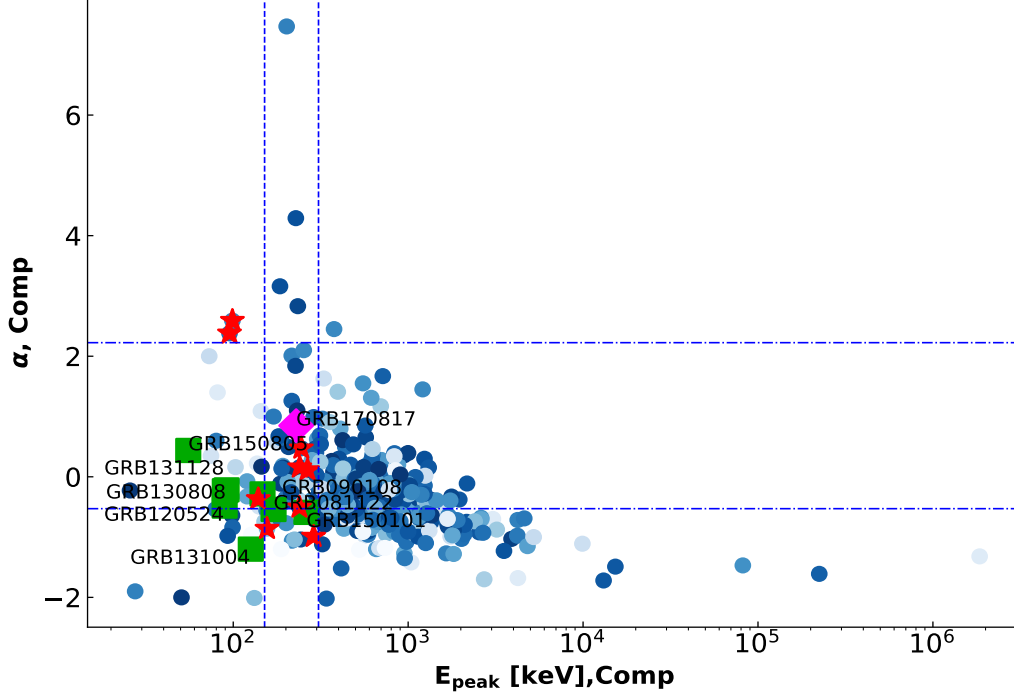


**Figure 1.** Scatter plot of Comp parameters from all archived sGRBs  $T_{90} < 2.05$  for the time-integrated spectrum. The sGRBs best fitted with PL and Comp are marked with light blue to dark blue  $T_{90}$  values, where dark blue indicates higher  $T_{90}$  values and lighter blue indicates lower  $T_{90}$ . The Comp parameters of sGRB 170817A are emphasized with a diamond (magenta color), the  $1\sigma$  error bars for  $E_{peak}$  are shown in dashed lines, and for the  $\alpha$  parameter, it is shown in dot-dashed lines. The eight possible sGRB 170817A-like bursts are marked with green squares. And sGRBs with known redshift are shown as stars (red color) (sGRB 150101B, sGRB 131004A are excluded).

(iii) The further sampling is implemented following the fact that the second peak,  $T_0 + 0.832$  sec to  $T_0 + 1.984$  sec (Zhang et al. (2018)) of sGRB 170817A has a blackbody (BB) spectral form,

$$F_{BB}(\epsilon_\gamma) = A \frac{\epsilon_\gamma^2}{\exp(\epsilon_\gamma/kT) - 1}, \quad (4)$$

with the thermal component at energy  $kT = 10.3 \pm 1.5$  keV for the second peak, where  $k$  is the Boltzmann constant. This sGRB has the  $T_{90}$  start time and end time as  $T_{90}^{\text{start}} = -0.192$ ,  $T_{90}^{\text{end}} = 1.856$ , respectively whereas the  $T_{50}^{\text{end}}$  time,  $T_{50}^{\text{end}} = 1.216$ , we chose to split the entire GRB time into two zones, Zone-A:  $T_{90}^{\text{start}}$  till  $T_{50}^{\text{end}}$  and Zone-B:  $T_{50}^{\text{end}}$  till  $T_{90}^{\text{end}}$ , so that the two zones can accommodate the first peak and the second peak. We calculated the HRs, which

are the ratios of the counts or flux in a high-energy band to that in a low-energy band, providing insight into the spectral characteristics of GRBs as a color index in the photometry. The HR provides insights into the energy distribution of the burst's emitted photons, which help distinguish between different types of GRBs and understanding their underlying physical mechanisms. By normalizing the exposure-corrected count numbers in two energy bands, HR is computed. The energy bands are, Low-energy band: 10-50 keV and High-energy band: 50-300 keV, within these two energy bands we calculate the HR in the aforementioned two time zones for the above selected 80 sGRBs, following the definition of the HRs as,

$$HR_1 = \frac{\text{photons within 50 to 300 keV in Zone-A}}{\text{photons within 10 to 50 keV in Zone-A}} \quad (5)$$

and,

$$HR_2 = \frac{\text{photons within 50 to 300 keV in Zone-B}}{\text{photons within 10 to 50 keV in Zone-B}}. \quad (6)$$

The values of the two HRs for these 80 sGRBs are listed in table 4 and shown in a scattering plot in Figure 2. The detailed calculation of the HR from the Fermi-GBM data is explained in section 4.

<sup>3</sup>  $T_{50}$  is the duration in which the central 50% of the gamma-ray signal is detected.

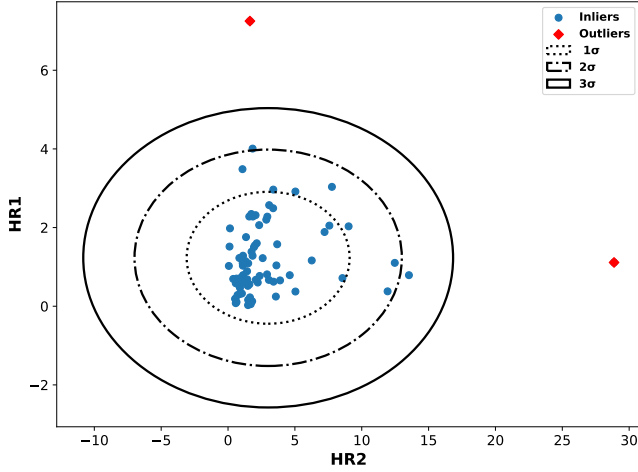


**Figure 2.** Distribution of data points in the  $HR_1$  &  $HR_2$  parameter space is displayed via a Mahalanobis distance plot. The ellipse show confidence contours that were obtained using the data's covariance. Dots (Blue color) represent the inliers (data used for further processing), while diamonds (red color) represent the outliers.

(iv) In a further step, we look for clusters within the HR scattering. However, before searching for such subgroups, we tried to eliminate the outliers to minimize bias. The outliers are identified using the Mahalanobis distance ( $D_m$ ) (Mahalanobis 2018). It is a multivariate distance metric that measures the separation between a data point and the distribution's mean, considering correlations between the variables. In contrast to simple Euclidean distance, it incorporates the covariance matrix to account for the data's orientation and shape.  $D_m$  (De Maesschalck et al. 2000) is written as follows :

$$D_m(\mathbf{x}) = \sqrt{(\mathbf{x} - \boldsymbol{\mu})^T \mathbf{S}^{-1} (\mathbf{x} - \boldsymbol{\mu})} \quad (7)$$

where  $\mathbf{x}$  is a data point,  $\boldsymbol{\mu}$  is the mean of the distribution, and  $\mathbf{S}$  is the covariance matrix of the dataset. Using this method, we draw the  $1\sigma$ ,  $2\sigma$ , and  $3\sigma$  standard deviation ellipses with dotted, dot-dashed, and solid lines, respectively, as shown in figure 2. If the data point falls outside the  $3\sigma$  range, it will be considered an outlier to the group. With the mentioned criteria, we find that sGRB 081101 and sGRB 120814 are the two outliers in our dataset as shown in Figure 2 as diamonds (red).

(v) In the scattering distribution of the 78 GRBs over their  $HR_1$  and  $HR_2$  values, we searched for subgroups in this step. We employed the K-means clustering algorithm for this purpose and found 6 possible clusters formed by the aforementioned 78 sGRBs. The details of the K-means adoption are explained in section 4.1. Out of the 6 clusters, cluster 1 as shown in the figure 3 contained sGRB 170817A along with the other 17 sGRBs, which are our final list of sGRBs to do the full light curve and spectral analysis. above, we finally made alike sGRBs set based on the following two steps. a) presence of distinct double peaks in the light curve, a feature suggesting off-axis sGRBs, b) followed by the BB emission fitting for the Zone-B spectral with energy,  $kT < 12$  keV, to look similar energy of sGRB 170817A. Out of these 17 sGRB, we found 8 sGRBs, sGRB 150805746, sGRB 150101641, sGRB 131128629, sGRB 131004904, sGRB 130808253, sGRB 120524134, sGRB 090108020, and sGRB 081122614 to satisfy the above-mentioned criteria and these details are mentioned in the table 5 and these 8

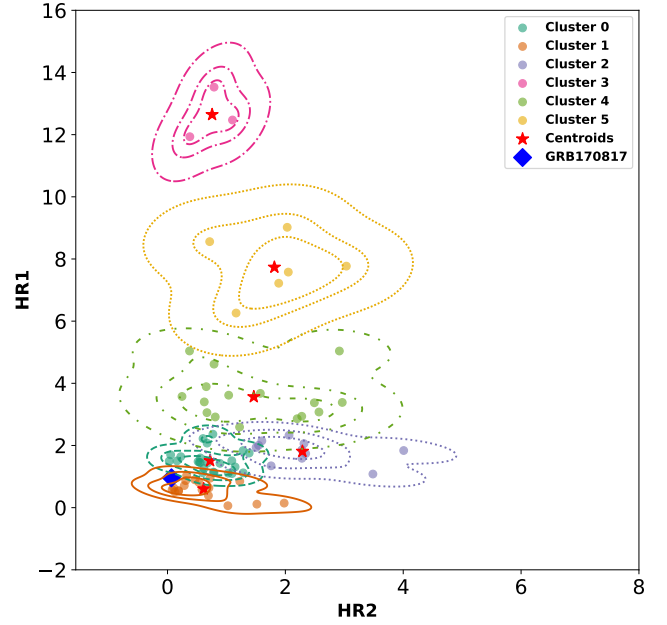


**Figure 3.** Contour based clustering ( $HR_1$  v/s  $HR_2$ ) at  $k = 6$ , each cluster represented by a distinct color. Contour lines indicate the density distribution of points within each cluster, which visually represents the data's structure, highlighting regions with higher concentrations of data points. Stars (red color) are centroids, the diamond (blue color) is sGRB 170817A.

alike sGRBs are with a superscript of a solid star. We show the lightcurve of these 8 sGRBs along with the sGRB 170817A in figure 6, calling them as the alike sGRBs to sGRB 170817A. A detailed analysis method is presented in Section 4.2. We have shown the spectral fitting parameters for the Comp model in Zone-A and the BB model in Zone-B for all the 80 sGRBs collected after the second step of the data selection procedure, in table 5.

A schematic diagram of the above mentioned selection procedure of alike sGRBs to the sGRB 170817A, is demonstrated in figure 4.

#### 4 $HR_1$ AND $HR_2$ CALCULATIONS

As defined in section 3, the  $HR_1$  &  $HR_2$  are the ratio of photon counts observed within energies 50 keV to 300 keV and 10 keV to 50 keV in time Zone-A and Zone-B, respectively. These parameters generally indicate the spectral transition of the GRBs through the total time of emission. We calculated the  $HR_1$  &  $HR_2$  for the 80 sGRBs selected in the second step of the data selection criteria, using a forward-folding spectral analysis software RMFIT – v4.3.2 package<sup>4</sup> (Mallozzi et al. (2005)).

The main purpose of RMFIT is to obtain the best-fit parameters for a chosen model from data files that include observed count rates (PHA files: photon count rate files), a matching detector response matrix file (RMF), and an auxiliary response file (ARF). For our case, we used Time-Tagged Event (TTE) data files, which have 128 energy channels with varying time bins. We utilized the graphical user interface of RMFIT to time- or energy-bin the files and determine the background, then saved both the signal and background files in ASCII format. From these files, we calculated the  $HR_1$  and  $HR_2$

<sup>4</sup> <https://fermi.gsfc.nasa.gov/ssc/data/p7rep/analysis/rmfit/>

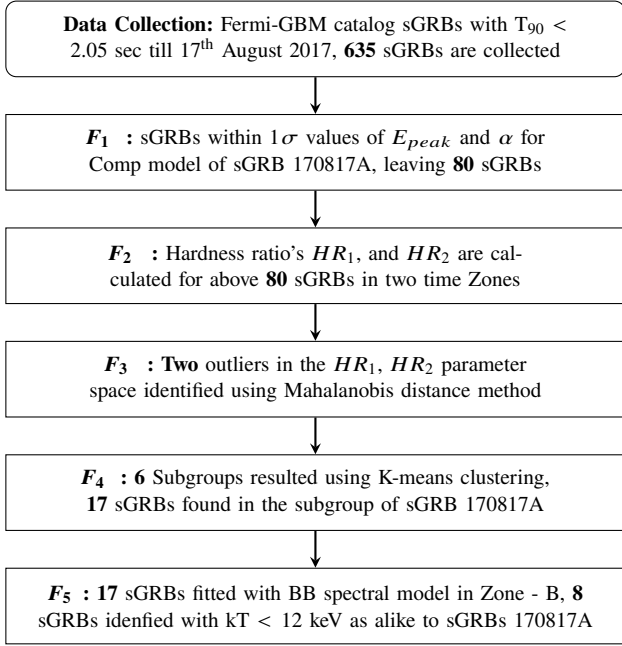


**Figure 4.** Workflow illustrating our process of finding out the twin sGRBs alike sGRB 170817A. **F** refers to the various filtering phases followed.

using the two most intense NaI detectors (Thallium-activated sodium iodide detector) mentioned in the burst catalog. Using the ASCII files generated from the TTE files, all the photon counts over the selected energy range will be added for the chosen two NAI detectors after subtracting the background. Then we calculated the  $HR_1$  and  $HR_2$  for the 80 sGRBs as selected in the second step of the data selection procedure, and listed the values in table 4 with the obtained photon counts along with the time zones, selected detectors, and redshift values (if available) of all 80 sGRBs.

#### 4.1 Subgroups in $HR_1$ vs $HR_2$ using K-Means Clustering

An in-depth understanding of the uniqueness or similarity with sGRB 170817A can be obtained by looking at the  $HR_1$  versus  $HR_2$  distribution of the 78 selected sGRBs. One of the most widely used unsupervised clustering techniques is K-means clustering (Lloyd (1982); MacQueen (1967); Na et al. (2010); Jin & Han (2011)). Here, we used this technique to search for further sub-grouping in the final dataset. The selection of the optimal number of clusters (K) is one of the primary tasks. Although determining K is not necessarily a clear-cut exercise, especially when the data is unlabeled. However, heuristic approaches coupled with a good understanding of the data set and its features are sufficient to determine a range of optimal values of K. For this task, numerous initializing strategies are available. We used the elbow method (Syakur et al. (2018); Umargono et al. (2020); Cui et al. (2020)) to find out the optimal number of K. For that, we have calculated the inertia (sum of the squared distances of each point to its assigned centroid). Inertia of a cluster can be calculated as the,

$$Inertia = \sum_{i=1}^N \sum_{j=1}^K \min(\|x_i - \mu_j\|^2) \quad (8)$$

where  $x_i$  are the data points in the cluster,  $\mu_i$  is the centroid of the cluster, and N & K are the set of data points and the number of clusters, respectively. In our case, we have calculated the inertia value

for various K values from 2 to 35. The value of the minimum inertia calculated using equation 8 is our optimal K, which is called the elbow (knee point) (Del Vecchio et al. 2016a; Antunes et al. 2018).

Although it is ideal to discover the point at which the line bends (forming an elbow shape) to obtain an accurate estimation of the K value. Most real data sets have a smooth curve, making it impossible to find the optimal K value. This is true for our case, as shown in figure 5. Since the elbow feature is not clear for our data set, therefore, to find the optimal K value, we used the Kneedle algorithm<sup>5</sup> (Satopaa et al. 2011; Qumsiyeh & Sabha 2023; Schubert 2023; Fok & Ye 2024)). This algorithm is a generic tool that uses K versus the inertia curve to detect the optimal K value for clustering tasks. It relies on the mathematical concept of curvature to measure how much a curve deviates from a straight line. Here, we identify the point of maximum curvature (finding the local maxima in a set of points), which occurs when the curvature decreases and the curve becomes flatter. Using this method, we found that the ideal number of clusters, K, is 6, shown with a vertical dashed line in figure 5. Furthermore, the kneedle point does not vary up to K = 35, since 35 is a huge number for our dataset, so we ignored it.

Once the optimal number of clusters is known, we proceed with calculating the distance from each data object to all the centers for the K-number of clusters.

In general, euclidean distance between two data points is calculated as follows: suppose we have two data points a and b in euclidean space of n-dimensional length, where a and b are  $a = (a_1, a_2, \dots, a_n)$ ,  $b = (b_1, b_2, \dots, b_n)$  then euclidean distance  $d(a, b)$  can be written according to (Na et al. 2010).

$$d(a_i, b_i) = \left[ \sum_{i=1}^n (a_i - b_i)^2 \right]^{1/2} \quad (9)$$

In K-means clustering, calculating the criterion function (J) or the cost function (Li & Wu 2012; Na et al. 2010) is a crucial step in labeling the data points with a particular cluster. It is defined as the sum of squared distances between data points with their respective centroids in all the K-number of clusters;

$$J = \sum_{i=1}^K \sum_{x \in C_i} |x - x_i|^2 \quad (10)$$

This parameter is calculated for several iterations. In each iteration, the mean distance of the cluster points from their respective centroids is calculated, followed by the relocation of the centroids. This method continues until the cluster centroids remain unchanged for two consecutive successful iterations or the value of the criterion function (or the cost function) falls below a specific threshold value. This point is considered to be the case where the algorithm has converged or stabilized. In this work, this threshold value is set to  $10^{-4}$ . We clustered our data using K = 6 to find clear patterns in the final dataset and examined the resulting groups. Figure 3 visually represents the results of the clustering, with contours that emphasize the density distribution of the data points and different colors for each cluster. Our root sGRB 170817A, visualized with the blue diamond, lies in cluster 1, which is brown in color; there are a total of 17 sGRBs in cluster 1. Interestingly, 8 out of 17 sGRBs in the cluster satisfies the selection criteria mentioned above. This clustering result strongly suggests us that these sGRBs share comparable traits, making the cluster especially pertinent for further research.

<sup>5</sup> <https://www.kaggle.com/code/kevinarvai/knee-elbow-point-detection>

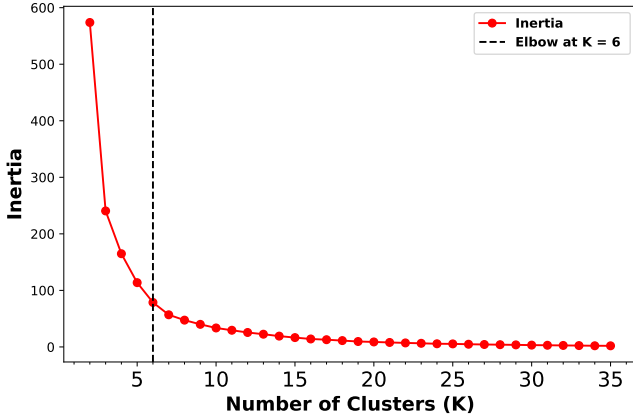


**Figure 5.** Variation of the inertia with the number of clusters. The black dashed line is the kneedle point representing the maximum curvature, corresponding to the optimal K number

## 4.2 LIGHT-CURVES & SPECTRAL ANALYSIS

This time, to precisely understand the similarity within the sGRB subgroup above, we perform temporal and spectral analysis using the GBM data. We discussed previously that the light curve of sGRB 170817A has two distinct features in both the temporal evolution and spectral form. For completeness, we analyzed these 80 sGRBs along with sGRB170817A using RMFIT analysis with the publicly available Fermi-GBM TTE data.

In the data collection step for the analysis, we selected only the two NaI detectors for which the position of the GRB is within  $60^\circ$  (Good geometry) and has the highest intensity, as discussed in section 4. Data are collected for energy channels 8 keV to 1 MeV, excluding channels around  $\sim 30-40$  keV (Kaneko et al. 2006; Jiang et al. 2025) because of iodine K-edge at 33.17 keV for NaI detectors. In order to subtract the background from the GBM data, we fitted data from two time interval values before and after the GRB prompt emission (around the selected time interval, i.e.,  $T_{90}$ ) with a polynomial as the background model (for lightcurve analysis, see : (Salafia et al. 2016; Del Vecchio et al. 2016b; Kumar & Sharma 2024). We defined the signal above the background by interpolating this polynomial around the GRB prompt phase.

We studied the light curve of the 8 sGRBs selected following section 3, similar to sGRB 170817A. For reference, we have also shown the same analysis result for sGRB 170817 figure 6. The figure includes LCs for different energy ranges 10-350 keV, 10-50 keV, 50-350 keV, from bottom to top. We show the two time zones with red (solid lines) and green (dot-dashed lines), respectively.

We performed the integrated spectral analysis for the two zones. To have an unbiased comparison, we have also analyzed sGRB 170817A using the same method, and the corresponding results are listed in table 5, which contains spectral analysis parameters for all the 79 sGRBs initially collected. We have highlighted the 8 sGRBs mentioned above with bold letters and superscript-star symbol in the table 5.

According to our analysis, the spectrum of the Zone-A of sGRB 170817A follows the Comp model with  $E_{\text{peak}} = 176.3 \pm 85.7$  keV and  $\alpha = 0.93 \pm 0.16$ . The Comp spectral Castor C statistic (C-stat) improvement (Cash 1979) of 3.21 therefore, has a chance of occurrence  $\sim 7.31 \times 10^{-2}$  compared to PL. The second peak spectrum follow BB with  $kT = 9.23 \pm 1.83$ . The C-stat spectral value of BB improves by 8.91 compared to the PL fit corresponding to a chance

of occurrence  $\sim 2.83 \times 10^{-3}$ . The number of variable parameters in BB is the same as for the PL function, and hence the result gives a statistically significant choice for the spectra to be BB radiation. We have also checked our analysis considering the same time zones for sGRB 170817A as in (Von Kienlin et al. 2019) and found negligible variation in results.

In addition, references (Burns et al. 2018b; Troja et al. 2017) also claimed sGRB 150101B as a luminous version of sGRB 170817A with a redshift of 0.1341. This GRB also belongs to one of the 8 sGRBs we have listed. Spectral analysis showed that the first zone from  $T_0 - 0.016$  to  $T_0 - 0.0$  s follows Comp with  $E_{\text{peak}} = 162.8$  and  $\alpha = 0.96$  over PL with a chance of occurrence only 0.05. And the soft tail within  $T_0 - 0.0$  to  $T_0 \pm 0.064$  has a spectral fit of BB with  $kT = 10.58$  preferred over PL with a chance of occurrence 0.03.

## 5 RESULTS AND DISCUSSIONS

We have studied the sGRBs observed by Fermi-GBM to identify GRBs similar to the only significant EM counterpart of the GW event observed to date, sGRB 170817A. It is one of the lowest-luminance GRBs observed to date, with a distance of only  $\sim 42$  Mpc. This sGRB shows unique and significant features in both the light curve and the spectral form of the observation. The primary emission (first zone) follows the Compton emission form, whereas in the later stage (second zone), the emission is dominated by BB radiation. Importantly, the two zones are separated by a distinctive time difference of 0.576 sec (as shown in table 3 of (Goldstein et al. 2017)). The time resolution for such a gap may not be identified for other GRBs. Hence, in our study, we focused solely on the visibility of the two distinct spectral forms. Our search resulted in eight sGRBs that may have alike origin, in the Fermi-GBM catalog observed from 17 July 2008 to 17 August 2017.

The statistical steps of this study are: We searched for subgroups in the distribution of HR parameter space of the two time zones, Zone-A ( $T_{90}^{\text{start}}$  to  $T_{90}^{\text{end}}$ ) and Zone-B ( $T_{50}^{\text{end}}$  to  $T_{90}^{\text{end}}$ ) for all the GRBs similar in the spectral form to sGRB 170817A in their Zone-A. We have used K-means statistics for subgrouping. Although we employed the kneedle method as explained in the section 4.1 for identifying the number of subgroups in the data, we utilized the elbow method. The last part of our search includes the spectral analysis and light curve analysis of sGRBs, and we further identified the softer BB-emitting sGRBs in Zone-B, using RMFIT analysis. The light curves of the resulting eight events are shown in the figure 6.

Out of the eight events, we found that two have a narrow second peak time period  $\delta t_2 = T_{90}^{\text{end}} - T_{50}^{\text{end}}$  compared to the other six. Like for sGRB 150101B, and sGRB 081122, the second peak time period  $\delta t_2 = 0.064$  sec. Other sGRBs, such as sGRB 150805, sGRB 131128, sGRB 130808, sGRB 131004A, sGRB 120524, and sGRB 090108 have  $\delta t_2$  values of 0.64, 0.768, 0.128, 0.576, 0.448, and 0.384 sec, respectively adding the sGRB 170817A has the  $\delta t_2 = 0.64$  sec.

For sGRB 150101B, and sGRB 131004A, with known redshift, we observed  $E_{\text{peak}} = 162.8$  keV and 107.3 keV, respectively from our analysis in the Zone-A. The remaining sGRBs, sGRB 150805, sGRB 131128, sGRB 130808, sGRB 120524, sGRB 090108, and sGRB 081122 have measured  $E_{\text{peak}}$  at 76.35 keV, 79.41 keV, 83.05 keV, 63.65 keV, 140.3 keV, and 143.8 keV, respectively, in zone A. The  $E_{\text{peak}}$  of sGRB 150101B, sGRB 131004A, sGRB 090108, and sGRB 081122 are similar to our root sGRB 170817A, where other GRBs are having a softer spectrum than the GRB 170817A.

In the case of GRB 170817A the integrated energy fluence for

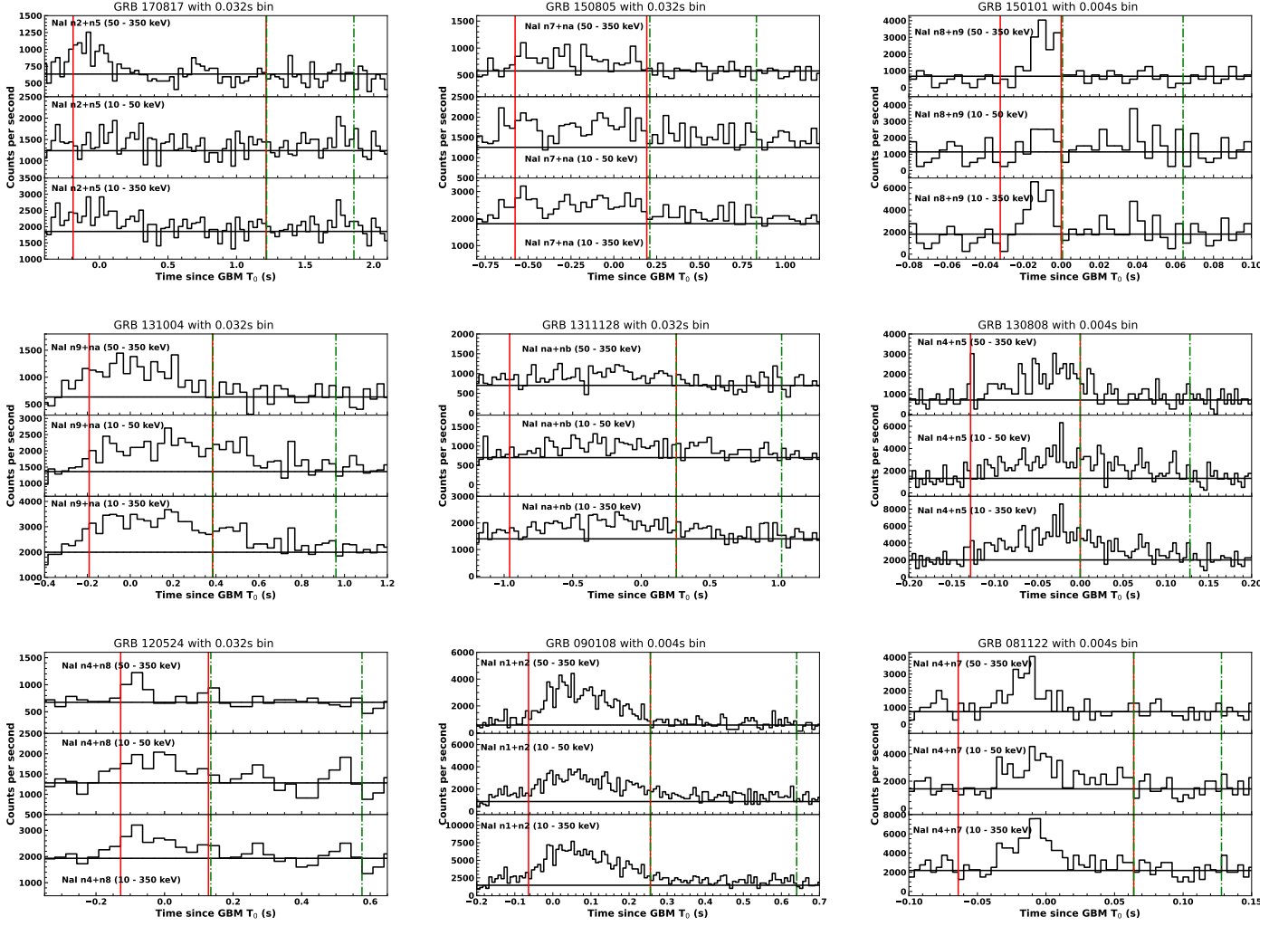


**Figure 6.** sGRBs similar to sGRB 170817A. The order of the light curves is the following: sGRB 170817A, sGRB 150805, sGRB 150101, sGRB 131128, sGRB 131004, sGRB 130808, sGRB 120524, sGRB 090108, and sGRB 081122. All the light curves are produced in the three energy ranges 50–350 keV, 10–50 keV and 10–350 keV with the binning size of 0.032 sec and 0.004 sec. The first and second peak time zones are shown with a solid (red) line and a dot-dashed (green) line, respectively. The light curve is the addition of the counts from the NAI detectors used for analysis. The horizontal solid (black) line is the background.

the Comp spectrum during Zone-A is  $1.20 \pm 0.4 \times 10^{-7}$  erg cm $^{-2}$  and the BB spectrum during Zone-B has value  $2.66 \pm 0.23 \times 10^{-8}$  erg cm $^{-2}$ . The BB-spectrum for the second peak has energy (keV)  $9.23 \pm 1.83$  keV. While for the other sGRBs, sGRB 150805, sGRB 150101B, sGRB 131128, sGRB 130808, sGRB 131004A, sGRB 120524, sGRB 090108, and sGRB 081122 have energy (keV) values of 9.21 keV, 9.82 keV, 10.41 keV, 12.00 keV, 7.76 keV, 7.60 keV, 10.73 keV, 11.26 keV, respectively. The spectral analysis results of the sGRBs for both Zone-A and Zone-B are listed in the table 8. A similar dedicated search has also performed in (Von Kienlin et al. 2019). Their result yields a total of 13 candidates, including GRB170817A and the earlier reported similar burst, GRB 150101B (Burns et al. 2018a). Their search is focused on peak searches in the light curve, emphasizing the presence of a valley between two peaks. We found no correlation in our resulted sample with the nearby sample of sGRBs resulting from BNS merger events from reference (Von Kienlin et al. 2019), except GRB 150101B, since such a valley does not exist in the similar candidate GRB 150101B. Additionally, all the claimed candidates in reference (Von Kienlin et al. 2019) could not pass our

selection criteria F1 (see figure 1). Our search focuses on looking for spectral forms defined by the observed  $T_{90}$  and  $T_{50}$  of the sGRBs.

Observation of sGRB170817A surprised the high-energy astrophysics community with its rate,  $R = 680 - 1300$  Gpc $^{-3}$  yr $^{-1}$ . We attempted calculating the event rate considering the sample of the 8 sGRBs selected as twining sGRB 170817A. Unfortunately, only two events out of the sample have measured redshift, sGRB 150101B and sGRB 131004A. The non-availability of spectroscopic measurements for the other 6 sGRBs leads to uncertainty in the distance of these events. Hence we followed the concept of pseudo-redshift ( $Z_p$ ) as developed in reference (Atteia 2003; Pizzichini et al. 2006), known as the Amati relation (Amati et al. 2002), but widely used for long GRBs (LGRBs). In this relation, the distribution of  $E_{\text{peak}}$  (here, as calculated in Zone-A) and  $E_{\text{iso}}$  in the source rest frame ( $E_{\text{peak}}^i = (1+z)E_{\text{peak}}$ ) has linear relation.

$$E_{\text{peak}}^i = k \left( \frac{E_{\text{iso}}}{10^{52} \text{ erg}} \right)^m \text{ keV}, \quad (11)$$

here,  $k$  and  $m$  are the fitting constants, and  $E_{\text{iso}}$  is isotropic energy

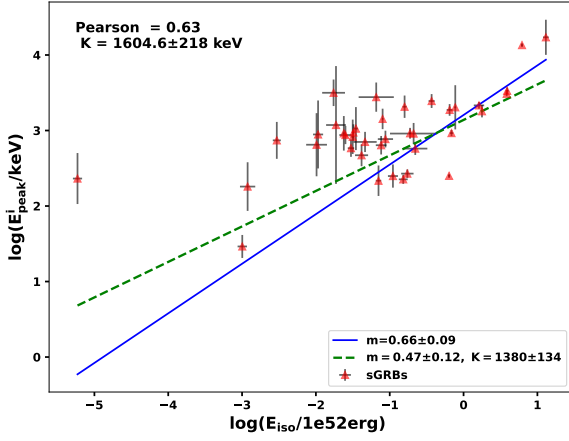


**Figure 7.** Correlation of  $E_{\text{iso}}$  with  $E_{\text{peak}}$  of Fermi-GBM sGRBs with known redshift till 17 August 2017.

which can be written as,  $E_{\text{iso}} = \frac{4\pi d_L^2}{1+z} f$  erg,  $d_L$  is luminosity distance,  $f$  is the energy fluence with unit  $\text{erg cm}^{-2}$ . Using cosmological constants (Komatsu et al. 2009)  $\Omega_M = 0.27$ ,  $\Omega_\Lambda = 0.73$ ,  $H_0 = 70 \text{ km s}^{-1} \text{ Mpc}^{-1}$  one can calculate  $d_L = \frac{(1+z)c}{H_0} \left[ \int_0^z \frac{dz'}{\sqrt{\Omega_M(1+z')^3 + \Omega_\Lambda}} \right]$ .

The Amati relation has been well established for LGRBs. However, such linearity could not be verified for sGRBs (Zitouni et al. 2022). We have also shown the distribution plot of  $E_{\text{peak}}$  vs  $E_{\text{iso}}$  for all the sGRBs observed by Fermi-GBM with redshift up to the detection of sGRB 170817A, in figure 7. A Pearson's correlation coefficient ( $r$ ) of 0.63 could be established on fitting a linear line similar to Amati relation, to these 40 sGRBs. the linear relation parameters are  $m = 0.66 \pm 0.09$  and  $k = 1604.6 \pm 218$ . This figure also clarifies, adding more data compared to reference (Zitouni et al. 2022), but still does not improve the result.

Recently, (Zitouni et al. 2022) reported statistically significant linearity in the Amati relation ( $E_{\text{peak}}$  vs  $E_{\text{iso}}$ ) using a joint sample of Fermi-GBM and Swift sGRBs. They obtained the best-fit parameters  $k = 1380^{+134}_{-121}$  and  $m = 0.47 \pm 0.12$ . The corresponding linear fit is shown as the dashed (green) line in their figure 7. Using this relation together with the fluence values of Zone-A derived from our Fermi-GBM analysis, we estimated the pseudo-redshifts for the six sGRBs in our sample. These pseudo-redshifts, along with the associated luminosity distances, are listed in Table 3 (marked with asterisks). The table also includes the two sGRBs with measured redshifts for comparison.

We estimate the event rate of sGRBs that resemble sGRB 170817A using their luminosity distances. The rate is calculated as,  $\frac{N}{tD(4\pi/3)d_L^3} \text{Gpc}^{-3} \text{yr}^{-1}$ , where  $t$  is the time span from 17 July 2008 to 17 August 2017. For simplicity, and due to the uncertainties in the redshift estimates, we take the number of events  $N$  to be one for each luminosity distance  $d_L$ . Figure 8 shows this rate with circles (blue color) representing the sGRBs with measured redshift ( $z$ ) and with the triangles (red color) indicate the sGRBs with calculated pseudo-redshift ( $z_p$ ).

The event rate clearly fits with a linear line to  $d_L$  as expected, shown with solid line in figure 8. We show the fitted relation as a solid green line, obtained using an ordinary least squares (OLS) fit, which yields a slope of  $-3.12 \pm 0.27$ , and an intercept of  $-3.42 \pm 0.43$ . Similarly, using the 11 sGRBs (Liu et al. 2025) in our dataset with

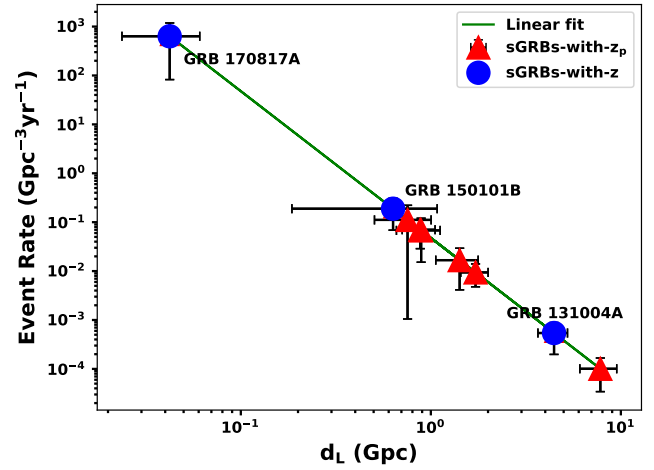


**Figure 8.** Luminosity distance vs Event rate of 8 sGRBs we found through our analysis with sGRB 170817A; circles (blue color) represent the sGRBs with measured redshift ( $z$ ) and triangles (red color) indicate the sGRBs with calculated pseudo-redshift ( $z_p$ ), green line is linear interpolation function fitted with data.

measured redshifts<sup>6</sup>, we computed their event rates as a function of luminosity distance and fitted the same functional form to this subset. The resulting slope and intercept are  $-3.01 \pm 0.11$  and  $-3.14 \pm 0.37$ , respectively.

Using the OLS function fitted above, we have constructed the formula for the possible number of multimessenger (GW+sGRB) events through LIGO and Fermi-GBM. The number of event are calculated for each observational run of, LIGO following,

$$N_{\text{GW+sGRB}} = 4\pi T \int_{d_{L\min}}^{d_{L\max}} d_L^2 f(d_L) d(d_L), \quad (12)$$

where  $T$  is the total operation time multiplied with the duty cycle of each run. The details of the duration of the run and the duty cycle are given in (Abbott et al. 2019, 2023b, 2024; The LIGO Scientific Collaboration et al. 2025).  $d_{L\max}$ ,  $d_{L\min}$  are upper and lower bounds of luminosity distances aimed at each run. We considered  $d_{L\min}$  as 10 Mpc and  $d_{L\max}$  as the maximum BNS observability limit for the respective observation run. We calculated the expected number of GW+sGRB events, for compact binary coalescence (CBC) mergers followed by EM counterparts corresponding to each observation run time,  $O_1$  to  $O_4$  for the LIGO-Virgo-KAGRA (LVK) interferometers. The details of the distance range for each run is listed in table 2. Details of the observability distance for the CBCs are explained in (Abbott et al. 2020a; Di Cesare 2025). The expected number of GW+sGRB events from the above calculation are listed in the table 2.

## 6 CONCLUSION AND OUTLOOK

With the first observation of the GW+sGRB event, sGRB 170817A the origin of sGRB as NS-NS CBC is confirmed. The large inclination, of  $\sim 33^\circ$  of the GRB jet resulted in a unique feature in the lightcurve, apart from the softer emission. Considering the soft

<sup>6</sup> <https://www.mpe.mpg.de/~jcg/grbgen.html>

**Table 2.** Expected number of GW+sGRB events from the LIGO all runs, operation time, and distance calculation, duty cycles are taken from (Abbott et al. 2020a; Di Cesare 2025; Capote et al. 2025)

Run	Time (Days)	Duty Cycle (%)	Distance ( $d_{L,max}$ ) (Mpc)	Expected number of GW+sGRB events
$O_1$	80.04	64.6	80	$0.58 \pm 0.05$
$O_2$	171.19	64.6	100	$1.36 \pm 0.17$
$O_{3a}$	127.09	71	110-130	$1.07 \pm 0.23$
$O_{3b}$	115.34	79	110-130	$0.97 \pm 0.12$
$O_{4a}$	169.452	71.2	160-190	$1.64 \pm 0.72$
$O_{4b}$	389.46	71.2	160-190	$3.77 \pm 1.46$

double peak structure of light curve we searched for sGRBs similar to sGRBs in the Fermi-GBM catalog, with a significant statistical approach. Our search yielded around 8 sGRBs including sGRB 150101B. resembling sGRB 170817A. This class of alike sGRBs could constitute the GW+sGRB events for sGRBs originated through NS-NS mergers. Using a pseudo-redshift method we calculated the possible number of events of GW+sGRB for sGRBs through NS-NS origin for different runs of the LIGO. Within  $O_1$  and  $O_2$  run the expected such events is  $0.58 \pm 0.05$  and  $1.36 \pm 0.17$  matches very well with the fact that sGRB 170817A was observed during  $O_2$  run. At the same time, the expected events in  $O_3$  and  $O_4$  run altogether give around 6 to 8 events. The possible CBC events reported through NS-NS and NS-BH mergers are GW190425 (Abbott et al. 2020b), GW190917\_114630 (Abbott et al. 2024) and GW200115\_042309 (Abbott et al. 2021). The upcoming  $O_5$  run is expected to begin in late 2027 and last for nearly two years. Taking into account the duty cycle of 73.73% (which is the average of the duty cycles of previous two observation runs). To estimate the expected duration of the  $O_5$  observing run, we applied the linear extrapolation method using the observed time duration of the previous all four completed runs ( $O_1$  to  $O_4$ ), we obtained an estimated  $O_5$  run time  $\sim 884$  days. Using these values, we calculated the expected number of  $N_{GW+sGRB}$  events for the distance range of 240 - 330 Mpc to be  $7.49 \pm 3.71$ .

## 7 ACKNOWLEDGEMENTS

We thank Soebur Razzaque for helpful discussions. Sanjeeva Rao would like to thank Neha Yadav (M.Sc. student).

## 8 DATA AVAILABILITY

All the sGRBs data used in this work were collected from the NASA HEASARC's Fermi-GBM burst catalog website, following link: [Fermi website](#). In support of this work, no additional data were generated or analyzed.

## REFERENCES

Abbott B. P., et al., 2017, *Phys. Rev. Lett.*, 119, 161101  
 Abbott B. P., et al., 2019, *Physical Review X*, 9, 031040  
 Abbott B. P., et al., 2020a, *Living Reviews in Relativity*, 23, 3  
 Abbott B. P., et al., 2020b, *Astrophys. J. Lett.*, 892, L3  
 Abbott R., et al., 2021, *Astrophys. J. Lett.*, 915, L5  
 Abbott R., et al., 2023a, *Phys. Rev. X*, 13, 011048  
 Abbott R., et al., 2023b, *Physical Review X*, 13, 041039  
 Abbott R., et al., 2024, *Phys. Rev. D*, 109, 022001  
 Amati L., et al., 2002, *A&A*, 390, 81

Antunes M., Ribeiro J., Gomes D., Aguiar R. L., 2018, in 2018 IEEE 6th international conference on future internet of things and cloud (FiCloud). pp 413–419  
 Atteia J.-L., 2003, *A&A*, 407, L1  
 Belczynski K., Taam R. E., Kalogera V., Rasio F. A., Bulik T., 2007, *ApJ*, 662, 504  
 Bhat P. N., et al., 2016, *Astrophys. J. Suppl.*, 223, 28  
 Burns E., Veres P., Mészáros P., Connaughton V., Briggs M. S., Goldstein A., et al., 2018a, *Astrophys. J. Lett.*, 863, L34  
 Burns E., et al., 2018b, *The Astrophysical Journal Letters*, 863, L34  
 Capote E., et al., 2025, *Phys. Rev. D*, 111, 062002  
 Cash W., 1979, *ApJ*, 228, 939  
 Coulter D. A., et al., 2017, *Science*, 358, 1556  
 Coward D. M., et al., 2012, *MNRAS*, 425, 2668  
 Cui M., et al., 2020, *Accounting, Auditing and Finance*, 1, 5  
 De Maesschalck R., Jouan-Rimbaud D., Massart D. L., 2000, *Chemometrics and intelligent laboratory systems*, 50, 1  
 Del Vecchio R., Dainotti M. G., Ostrowski M., 2016a, *The Astrophysical Journal*, 828, 36  
 Del Vecchio R., Dainotti M. G., Ostrowski M., 2016b, *Astrophys. J.*, 828, 36  
 Di Cesare M., 2025, arXiv preprint arXiv:2505.18802  
 Drout M. R., et al., 2017, *Science*, 358, 1570  
 Eichler D., Livio M., Piran T., Schramm D. N., 1989, *Nature*, 340, 126  
 Evans P. A., et al., 2017, *Science*, 358, 1565  
 Fok T. Y., Ye N., 2024, arXiv preprint arXiv:2409.15608  
 Fong W., et al., 2017, *Astrophys. J. Lett.*, 848, L23  
 Goldstein A., et al., 2017, *ApJ*, 848, L14  
 Granot J., Gill R., Guetta D., De Colle F., 2018, *Mon. Not. Roy. Astron. Soc.*, 481, 1597  
 Gruber D., et al., 2014, *Astrophys. J. Suppl.*, 211, 12  
 Hayes F., Heng I. S., Lamb G., Lin E.-T., Veitch J., Williams M. J., 2023, *Astrophys. J.*, 954, 92  
 Howell E. J., Ackley K., Rowlinson A., Coward D., 2019, *Mon. Not. Roy. Astron. Soc.*, 485, 1435  
 Jiang L.-Y., et al., 2025, *Nature Communications*, 16, 2668  
 Jin X., Han J., 2011, *Encyclopedia of machine learning*, pp 563–564  
 Kalogera V., Narayan R., Spergel D. N., Taylor J. H., 2001, *Astrophys. J.*, 556, 340  
 Kalogera V., et al., 2004, *Astrophys. J. Lett.*, 601, L179  
 Kaneko Y., Preece R. D., Briggs M. S., Paciesas W. S., Meegan C. A., Band D. L., 2006, *AIP Conf. Proc.*, 836, 133  
 Kapadia S. J., Dimple Jain D., Misra K., Arun K. G., Lekshmi R., 2024, *Astrophys. J. Lett.*, 976, L10  
 Komatsu E., et al., 2009, *Astrophys. J. Suppl.*, 180, 330  
 Kumar A., Sharma K., 2024, arXiv e-prints, p. arXiv:2411.13242  
 Li Y., Wu H., 2012, *Physics Procedia*, 25, 1104  
 Liu Y., Zhang Z.-B., Dong X.-F., Li L.-B., Du X.-Y., 2025  
 Lloyd S., 1982, *IEEE transactions on information theory*, 28, 129  
 MacQueen J., 1967, in *Proceedings of the Fifth Berkeley Symposium on Mathematical Statistics and Probability*, Volume 1: Statistics. pp 281–298  
 Mahalanobis P. C., 2018, *Sankhyā: The Indian Journal of Statistics, Series A* (2008-), 80, S1  
 Mallozzi R., Preece R., Briggs M., 2005, *Univ. Alabama, Huntsville*  
 Margalit B., Metzger B. D., 2017, *ApJ*, 850, L19  
 Margutti R., et al., 2017, *ApJ*, 848, L20  
 Mazwi L., Razzaque S., Nyadzani L., 2024, *Mon. Not. Roy. Astron. Soc.*, 531, 2162  
 Meegan C. A., Koshut T. M., Preece R. D., eds, 1998, *Proceedings, 4th Huntsville Symposium: Gamma-Ray Bursts: Huntsville, USA, September 15-20, 1997* Vol. 428  
 Mooley K. P., et al., 2018, *Nature*, 561, 355  
 Na S., Xumin L., Yong G., 2010, in 2010 Third International Symposium on intelligent information technology and security informatics. pp 63–67  
 Narayan R., Piran T., Shemi A., 1991, *Astrophys. J. Lett.*, 379, L17  
 Narayan R., Paczynski B., Piran T., 1992, *Astrophys. J. Lett.*, 395, L83  
 Pandey S., Gupta I., Chandra K., Sathyaprakash B. S., 2025, *Astrophys. J. Lett.*, 985, L17  
 Pian E., et al., 2017, *Nature*, 551, 67

- Pizzichini G., Ferrero P., Genghini M., Gianotti F., Topinka M., 2006, [Advances in Space Research](#), **38**, 1338
- Poggiani R., et al., 2020, POS PROCEEDINGS OF SCIENCE, 362
- Poolakkil S., et al., 2021, [Astrophys. J.](#), 913, 60
- Porciani C., Madau P., 2001, [Astrophys. J.](#), 548, 522
- Qumsiyeh E., Sabha M., 2023, in 2023 2nd International Engineering Conference on Electrical, Energy, and Artificial Intelligence (EICEEAI). pp 1–7
- Salafia O. S., Ghisellini G., Pescalli A., Ghirlanda G., Nappo F., 2016, [Mon. Not. Roy. Astron. Soc.](#), 461, 3607
- Satopaa V., Albrecht J., Irwin D., Raghavan B., 2011, in 2011 31st international conference on distributed computing systems workshops. pp 166–171
- Schubert E., 2023, ACM SIGKDD Explorations Newsletter, 25, 36
- Smartt S. J., et al., 2017, [Nature](#), 551, 75
- Syakur M. A., Khotimah B. K., Rochman E., Satoto B. D., 2018, in IOP conference series: materials science and engineering. p. 012017
- Tanvir N. R., et al., 2017, [ApJ](#), **848**, L27
- The LIGO Scientific Collaboration et al., 2025, [arXiv e-prints](#), p. [arXiv:2508.18080](#)
- Troja E., et al., 2017, [Nature](#), 551, 71
- Umargono E., Suseno J. E., Gunawan S. V., 2020, in The 2nd international seminar on science and technology (ISSTEC 2019). pp 121–129
- Villar V. A., et al., 2017, [ApJ](#), **851**, L21
- Von Kienlin A., et al., 2019, The Astrophysical Journal, 876, 89
- Zhang B. B., et al., 2018, [Nature Commun.](#), 9, 447
- Zitouni H., Guessoum N., Azzam W., 2022, [Ap&SS](#), **367**, 74
- von Kienlin A., et al., 2019, [ApJ](#), **876**, 89

**Table 3.** Pseudo-redshift, luminosity distance,  $E_{peak}^i$ ,  $E_{iso}$ , and Energy fluence ( $E_f$ ) for the sGRBs without redshift. \*The sGRBs with known redshift.

Name	$z$ or $z_p$	$d_L$ (Gpc)	$E_{peak}^i$ (keV)	$E_{iso}$ (erg) $\times 10^{48}$	$E_f$ (Zone - A) (erg/cm <sup>2</sup> ) $\times 10^{-7}$	$E_f$ (Zone - B) (erg/cm <sup>2</sup> ) $\times 10^{-7}$	Chances of occurrence (10 <sup>-2</sup> )
GRB 170817529*	0.009783 $\pm$ 0.0071	0.0422 $\pm$ 0.018	178.02 $\pm$ 78.87	0.059 $\pm$ 0.003	1.20 $\pm$ 0.40	0.266 $\pm$ 0.02	0.28
GRB 150805746	0.18 $\pm$ 0.03	0.87 $\pm$ 0.17	90.10 $\pm$ 12.50	31.75 $\pm$ 10.24	3.40 $\pm$ 0.37	1.10 $\pm$ 0.19	0.25
GRB 150101641*	0.134 $\pm$ 0.058	0.6330 $\pm$ 0.454	184.61 $\pm$ 10.70	10.06 $\pm$ 0.63	0.26 $\pm$ 0.18	0.21 $\pm$ 0.07	3.29
GRB 131128629	0.15 $\pm$ 0.04	0.75 $\pm$ 0.24	91.79 $\pm$ 22.24	35.70 $\pm$ 20.99	2.20 $\pm$ 0.23	0.82 $\pm$ 0.15	3.12
GRB 131004904*	0.717 $\pm$ 0.130	4.4529 $\pm$ 0.789	184.23 $\pm$ 76.31	704.83 $\pm$ 26.39	4.66 $\pm$ 0.67	0.86 $\pm$ 0.13	10.48
GRB 130808253	0.27 $\pm$ 0.05	1.41 $\pm$ 0.35	105.80 $\pm$ 18.66	46.41 $\pm$ 22.03	3.10 $\pm$ 0.72	1.1 $\pm$ 0.21	0.28
GRB 120524134	0.18 $\pm$ 0.04	0.88 $\pm$ 0.23	75.20 $\pm$ 14.11	21.73 $\pm$ 10.36	2.69 $\pm$ 0.28	0.37 $\pm$ 0.07	0.55
GRB 090108020	0.32 $\pm$ 0.04	1.71 $\pm$ 0.28	185.83 $\pm$ 20.05	143.60 $\pm$ 41.01	0.78 $\pm$ 0.12	0.74 $\pm$ 0.07	3.12
GRB 081122614	0.93 $\pm$ 0.16	7.97 $\pm$ 1.71	277.60 $\pm$ 35.55	1132.90 $\pm$ 246.20	0.61 $\pm$ 0.19	0.04 $\pm$ 0.004	3.40

**Table 4:** Hardness ratio's,  $HR_1$  and  $HR_2$  of all the sGRBs listed in our final set of data. Associated times ( $T_{90}, T_{50}$ ) and detectors that we considered for analysis. Along with the redshift value in the last column.

NOTE: \* We did not consider the GRB for K-means clustering.

GRBs	$T_{90}^{start}$ (s)	$T_{50}^{end}$ (s)	$T_{90}^{end}$ (s)	Detectors	$HR_1$	$HR_2$	Redshift value( $z^c$ )
GRB170817529	-0.192	1.216	1.856	n2, n5	0.578	0.0784	0.009783h
GRB170726249	-0.768	0.512	1.024	n7, n9	1.508	1.0911	-
GRB170511648	-1.28	-0.512	0	n6, n11	1.587	2.280	-
GRB170304003	-0.016	0.048	0.144	n1, n9	2.222	0.6029	-
GRB161026373	-0.032	0.032	0.080	n0, n3	1.440	0.682	-
GRB160826938	-1.344	-0.192	0.448	n1, n2	0.809	0.534	-
GRB160821937	-0.064	0.32	1.024	n9, n11	0.0616	1.024	0.16h
GRB160603719	-0.128	0.128	0.256	n7, n8	3.617	1.038	-
GRB160411062	-0.928	-0.384	-0.256	n4, n8	1.598	0.557	-
GRB160224911	-0.064	0.320	0.320	n1, n5	13.529	0.7897	-
GRB151229486	-0.064	0.032	0.096	n3, n4	3.401	0.624	1.4ph
GRB150923864	0	1.088	1.792	n7, n8	1.120	1.2847	-
GRB150923429	-0.064	0.064	0.128	n4, n9	12.471	1.102	-
GRB150912600	-0.128	0.192	0.192	n1, n2	11.934	0.379	-
GRB150901924	-0.064	0.064	0.192	n10, n11	3.384	2.965	-
GRB150805746	-0.576	0.192	0.832	n7, n11	0.534	0.187	-
GRB150705588	-0.256	0	0.448	n3, n7	1.121	0.595	-
GRB150628767	-0.064	0.256	0.576	n6, n8	5.039	2.916	-
GRB150609316	-0.240	-0.016	0.016	n0, n1	0.145	1.979	-
GRB150605782	-0.048	-0.016	0.128	n7, n8	1.142	0.780	-
GRB150412507	-0.128	0.128	0.448	n8, n9	1.0813	3.485	-
GRB150325696	-0.032	0.016	0.048	n6, n7	7.770	3.035	-
GRB150301045	-0.032	0.032	0.384	n4, n8	1.095	1.094	-
GRB150101270	-0.416	-0.032	0.064	n0, n3	0.589	3.82	-
GRB150101641	-0.016	0	0.064	n8, n9	1.805	0.126	0.134h
GRB141128962	-0.096	0.032	0.172	n2, n5	1.503	0.161	-
GRB141102112	-0.032	-0.016	-0.016	n6, n8	2.918	0.810	-
GRB140724533	-0.256	0.064	0.64	n8, n11	1.345	1.757	-
GRB140624423	-0.080	0.016	0.016	n3, n4	2.148	1.601	-
GRB140209313	1.344	1.856	2.752	n9, n10	1.4822	0.518	-
GRB131128629	-0.96	0.256	1.024	n10, n11	0.869	0.308	-
GRB131004904	-0.192	0.384	0.960	n9, n10	0.7065	0.635	0.717
GRB130919173	-0.064	0.768	0.896	n7, n8	0.947	0.722	-
GRB130808253	-0.128	0	0.128	n4, n5	0.710	0.284	-
GRB130622615	-0.768	0	0.192	n7, n8	1.108	1.031	-
GRB130617564	-0.448	0.064	0.32	n2, n10	1.835	1.283	-
GRB130404877	-0.128	0.192	0.832	n0, n1	1.639	0.225	-
GRB130325005	-0.064	0.192	0.576	n6, n7	3.676	1.575	-
GRB121004211	-0.512	0.512	1.024	n3, n4	0.847	1.226	-
GRB120831901	-0.256	0	0.128	n4, n5	1.855	2.280	-
GRB120814803*	-0.192	0	0	n4, n6	28.87	1.112	-
GRB120629565	-0.384	0.064	0.32	n3, n6	5.040	0.373	-

r

Continued on next page...

Table 4 (continued)

GRBs	$T_{90}^{\text{start}}$ (s)	$T_{50}^{\text{end}}$ (s)	$T_{90}^{\text{end}}$ (s)	Detectors	$HR_1$	$HR_2$	Redshift value( $z^c$ )
GRB120524134	-0.128	0.128	0.576	n4, n8	0.546	0.188	-
GRB120429003	-0.192	0.640	1.472	n10, n11	1.757	1.385	-
GRB120327418	-0.192	-0.064	0.064	n4, n8	0.063	3.076	2.813
GRB120222021	-0.064	0.576	1.024	n3, n5	1.123	0.789	-
GRB120101354	-0.096	0	0.032	n7, n8	1.701	0.053	-
GRB111207512	-0.896	-0.256	-0.128	n0, n1	8.557	0.715	-
GRB111117510	-0.064	0.352	0.368	n0, n9	2.328	2.062	2.21h
GRB111011094	-0.064	0.128	1.408	n8, n11	1.457	0.541	-
GRB111001804	-0.256	0	0.128	n7, n11	9.018	2.031	-
GRB110605780	-0.256	0.768	1.28	n8, n10	3.056	0.669	-
GRB110509475	-0.320	-0.064	0.320	n3, n5	1.448	0.556	-
GRB110227009	-0.192	0.640	1.536	n7, n8	3.577	0.246	-
GRB110131780	-0.192	0.064	0.192	n0, n1	7.219	1.887	-
GRB101216721	0.003	0.832	1.92	n1, n5	1.490	0.0628	-
GRB101208498	-0.640	0.640	1.408	n2, n5	0.387	0.694	-
GRB101027230	-1.280	0.064	0.064	n6, n7	3.892	0.657	-
GRB100816026	0.003	1.408	2.048	n8, n11	1.67	1.311	0.8035
GRB100805300	-0.096	-0.032	-0.032	n8, n10	2.061	2.315	-
GRB100629801	-0.128	0.320	0.704	n10, n11	1.259	0.618	-
GRB100616773	-0.192	-0.064	0	n9, n10	6.260	1.163	-
GRB100516396	-0.576	-0.064	0.064	n6, n7	3.374	2.490	-
GRB100417166	-0.064	0.064	0.128	n7, n9	2.364	0.770	-
GRB100117879	-0.064	0.064	0.192	n4, n8	2.938	2.278	0.92phh
GRB091126333	-0.064	0.064	0.128	n6, n11	2.860	2.200	-
GRB091019750	-0.112	-0.016	0.096	n1, n2	2.004	1.544	-
GRB091006360	-0.192	-0.064	0	n1, n2	2.592	1.223	-
GRB090927422	-0.192	0.192	0.32	n2, n10	1.938	1.503	1.37
GRB090616157	-0.192	0.512	0.960	n2, n5	0.893	0.465	-
GRB090518080	-0.640	0.768	1.408	n1, n3	0.1124	1.516	-
GRB090108020	-0.064	0.256	0.64	n1, n2	1.038	0.324	-
GRB081230871	-0.128	0.192	0.384	n7, n9	7.577	2.049	2ph
GRB081226044	-0.192	0.192	0.64	n2, n10	1.837	4.007	-
GRB081223419	-0.064	0.256	0.512	n7, n11	1.424	0.8896	-
GRB081122614	-0.064	0.064	0.128	n4, n7	0.634	0.702	-
GRB081107321	-0.192	1.152	1.472	n6, n9	0.577	0.585	-
GRB081101491*	-0.064	0.064	0.064	n9, n10	2.294	7.249	-
GRB080919790	-0.128	0.064	0.384	n0, n2	2.075	0.671	-
GRB080831053	-0.288	0	0.288	n0, n5	4.616	0.789	-

Table 5: Best fit parameters for all the 80 sGRBs from the final sample set. From left to right, the **first column** contains the name of GRB; in the **second column**, the first time interval is for the Zone-A that was observed in the GRB, which is fitted with the Comp model, and corresponding parameter values  $E_{\text{peak}}, \alpha$  are listed in the **fourth and fifth columns**, respectively. The second time interval is for the Zone-B that's seen in the GRB, which is fitted with the BB model, and the corresponding best fitted parameter values (kT) are given in the **sixth column**. In the **seventh column**, C-stat and degree of freedom (dof) values are noted to describe how well the model fits the data.

GRB Names	Time (s)	Model	$E_{\text{peak}}$ (keV)	Index	kT (keV)	C-stat/dof
GRB170817529	-0.192:1.216	Comp	$176.3 \pm 85.7$	$-0.9364 \pm 0.168$	-	247.55/231
	-0.192:1.216	PL	-	$-1.586 \pm 0.162$	-	248.64/232
	1.216:1.856	BB	-	-	$9.236 \pm 1.83$	263.06/232
	1.216:1.856	PL	-	$-2.140 \pm 0.482$	-	269.93/232
GRB170726249	-0.768:0.512	Comp	$481.4 \pm 398$	$-0.933 \pm 0.32$	-	210.31/227
	0.512:1.024	BB	-	-	$34.64 \pm 0.26$	243.3/228
GRB170511648	-0.08:0.016	Comp	$44.9 \pm 54.9$	$0.2861 \pm 1.5$	-	263.67/231
	0.016:0.016	BB	-	-	$56.03 \pm 15$	270.84/232
GRB170304003	-0.064:-0.016	Comp	$272.2 \pm 149$	$0.043 \pm 0.005$	-	196.81/229
	-0.016:0.032	BB	-	-	$5.233 \pm 0.03$	162.10/230

Continued on next page...

Table 5 (continued)

GRB Names	Time (s)	Model	Epeak (keV)	Index	kT (keV)	C-stat/dof
GRB161026373	-0.032:0.032	Comp	$324.6 \pm 181$	$-0.503 \pm 0.44$	-	229.1/228
	0.032:0.080	BB	-	-	$49.71 \pm 7.95$	269.6/229
<b>GRB160826938</b>	-1.344:-0.192	Comp	$99.90 \pm 22.2$	$-0.3554 \pm 0.49$	-	244.39/228
	-0.192:0.448	BB	-	-	$14.23 \pm 2.63$	271.67/229
<b>GRB160821937</b>	-0.064:0.32	Comp	$79.44 \pm 18.2$	$-0.9368 \pm 0.38$	-	267.04/228
	0.32:1.024	BB	-	-	$29.64 \pm 8.18$	253.01/229
GRB160603719	-0.128-0.128	Comp	$377.2 \pm 151$	$0.191 \pm 0.629$	-	296.9/228
	0.128-0.256	BB	-	-	$21.35 \pm 7.86$	232.87/229
GRB160411062	-0.384:-0.256	Comp	$83.76 \pm 15.9$	$-0.9362 \pm 0.31$	-	226.83/227
	1.344-1.664	BB	-	-	$9.550 \pm 1.15$	254.14/228
GRB160224911	-0.064:0.32	Comp	$308.9 \pm 188$	$0.045 \pm 0.012$	-	204.92/221
	0.32:0.32	BB	-	-	$46.34 \pm 59.1$	235.99/222
GRB150923864	0:1.088	Comp	$131.7 \pm 10.7$	$-0.243 \pm 0.15$	-	227.40/229
	1.088:1.792	BB	-	-	$25.89 \pm 1.91$	240.84/230
GRB150923429	-0.064:0.064	Comp	$229.8 \pm 103$	$0.0784 \pm 2.04$	-	217.55 / 221
	0.064:0.128	BB	-	-	$49.21 \pm 15.3$	182.54/222
GRB150912600	-0.128:0.192	Comp	$660.2 \pm 304.7$	$-0.463 \pm 0.274$	-	281.74/241
	0.192 :0.192	BB	-	-	$37.80 \pm 4.79$	282.67/242
GRB150901924	-0.08:0.016	Comp	$289.8 \pm 93.4$	$1.412 \pm 1.15$	-	224.46/225
	0.016:0.016	BB	-	-	$21.44 \pm 6.50$	202.61/226
<b>GRB150805746*</b>	-0.576:0.192	Comp	$76.35 \pm 14.7$	$1.226 \pm 0.28$	-	251.34/228
	0.192:0.832	BB	-	-	$9.201 \pm 4.72$	248.76/229
	0.192:0.832	PL	-	$-2.61 \pm 0.30$	-	257.83/229
GRB150705588	-0.256:0	Comp	$152.8 \pm 66.6$	$-0.9619 \pm 0.38$	-	219.12/226
	0:0.448	BB	-	-	$15.18 \pm 2.99$	232.97/227
GRB150628767	0.034:0.022	Comp	$267.7 \pm 75.8$	$0.630 \pm 0.812$	-	218.93/223
	0.256:0.576	BB	-	-	$62.74 \pm 13.6$	267.33/224
<b>GRB150609316</b>	-0.24:-0.016	Comp	$5457 \pm 1677$	$-1.034 \pm 0.786$	-	231.36/228
	-0.016:-0.016	BB	-	-	$39.04 \pm 5.46$	231.71/229
GRB150605782	-0.048:-0.016	Comp	$251.72 \pm 80.25$	$-0.369 \pm 0.06$	-	243.34/227
	-0.016:-0.128	BB	-	-	$44.47 \pm 7.30$	218.64/228
GRB150412507	-0.128:0.128	Comp	$89.75 \pm 28$	$-0.9054 \pm 0.54$	-	237.84/223
	0.128:0.448	BB	-	-	$16.08 \pm 6.23$	223.61/ 224
GRB150325696	-0.032:0.016	Comp	$248.5 \pm 63.5$	$0.599 \pm 0.65$	-	263.42/229
	0.016:0.048	BB	-	-	$43.89 \pm 6.03$	232.16/230
GRB150301045	-0.032:0.032	Comp	$257.6 \pm 128$	$-0.7496 \pm 0.41$	-	230.20/231
	0.032:0.384	BB	-	-	$14.76 \pm 4.14$	228.16/232
GRB150101270	-0.416:-0.032	Comp	$224.6 \pm 89.4$	$0.2787 \pm 0.08$	-	221.12/232
	-0.032:0.064	BB	-	-	$45.31 \pm 9.06$	241.44/233
<b>GRB150101641*</b>	-0.016:0	Comp	$162.8 \pm 18.3$	$-0.9619 \pm 0.29$	-	241.80/230
	0:0.064	BB	-	-	$9.828 \pm 4.15$	198.71/231
	0:0.064	PL	-	$-2.588$	-	203.26/231
GRB141128962	-0.096:0.032	Comp	$167.6 \pm 48.8$	$-0.489 \pm 0.381$	-	204.76/217
	0.032:0.176	BB	-	-	$13.06 \pm 1.17$	258.22/218
GRB141102112	-0.032:-0.016	Comp	$87.46 \pm 115$	$0.197 \pm 0.52$	-	305.82/253
	-0.016:-0.016	BB	-	-	$9.822 \pm 1.62$	280.88/254
GRB140724533	-0.256:0.064	Comp	$207.3 \pm 114$	$-0.696 \pm 0.480$	-	262.05/230
	0.064:0.64	BB	-	-	$29.05 \pm 12.2$	277.82/231
GRB140624423	-0.08:0.016	Comp	$260.6 \pm 95.6$	$-0.7626 \pm 0.30$	-	241.4/228
	0.016:0.016	BB	-	$-2.84$	$33.80 \pm 2.84$	223.54/221
GRB140209313	1.344:1.856	Comp	$189.1 \pm 51.8$	$-0.262 \pm 0.04$	-	292.8/227
	1.856:2.752	BB	-	-	$14.88 \pm 0.195$	217/228
<b>GRB131128629*</b>	-0.96:0.256	Comp	$79.41 \pm 51.33$	$0.086 \pm 0.13$	-	216.92/225
	0.256:1.024	BB	-	-	$10.41 \pm 0.97$	291.17/226
	0.256:1.024	PL	-	$-1.981$	-	295.81/226
<b>GRB131004904*</b>	-0.192:0.384	Comp	$107.3 \pm 30.1$	$-1.197 \pm 0.26$	-	230.44/225
	0.384:0.96	BB	-	-	$7.761 \pm 0.75$	250.22/226

Continued on next page...

Table 5 (continued)

GRB Names	Time (s)	Model	Epeak (keV)	Index	kT (keV)	C-stat/dof
	0.256:1.024	PL	-	$-2.31 \pm 0.20$	-	252.85/226
<b>GRB130919173</b>	-0.064:0.768	Comp	$141.5 \pm 28.6$	$-0.5225 \pm 0.313$	-	236.60/220
	0.768:0.896	BB	-	-	$18.04 \pm 1.63$	216.34/221
<b>GRB130808253*</b>	-0.128:0	Comp	$83.05 \pm 41.28$	$-0.11 \pm 0.05$	-	244.23/224
	0:0.128	BB	-	-	$12.00 \pm 5.17$	201.81/225
	0:0.128	PL	-	$-1.991 \pm 0.16$	-	210.69/225
GRB130622615	-0.768:0	Comp	$134 \pm 33.5$	$-0.531 \pm 0.39$	-	254.4/229
	0:0.192	BB	-	-	$31.89 \pm 5.45$	230.9/230
GRB130617564	-0.448:0.064	Comp	$1127 \pm 1000$	$-0.772 \pm 0.294$	-	216.39/223
	0.064:0.320	BB	-	-	$41.29 \pm 15.9$	257.94/224
GRB130404877	-0.128:0.192	Comp	$229.6 \pm 93.8$	$-0.032 \pm 0.073$	-	232.1/226
	0.192:0.832	BB	-	-	$73.24 \pm 32.7$	215.45/227
GRB130325005	-0.064:0.192	Comp	$231.5 \pm 87.4$	$1.98 \pm 1.67$	-	222.15/230
	0.192:0.576	BB	-	-	$47.21 \pm 16.13$	226.22/231
<b>GRB121004211</b>	-0.512:0.512	Comp	$125.8 \pm 29.9$	$-0.5616 \pm 0.35$	-	246.6/224
	0.512:1.024	BB	-	-	$19.62 \pm 2.21$	245.27/230
GRB120831901	502.1:431	Comp	$502.1 \pm 431.0$	$-0.330 \pm 0.690$	-	255.28/226
	0:0.128	BB	-	-	$49.89 \pm 7.05$	208.82/227
GRB120814803	-0.192:0	Comp	$170.2 \pm 38.4$	$2.647 \pm 2.81$	-	243.34/227
	0:0	BB	-	-	$64.88 \pm 21.56$	203.03/228
GRB120629565	-0.384:0.064	Comp	$200.8 \pm 89$	$0.325 \pm 0.157$	-	254.84/229
	0.064:0.320	BB	-	-	$18.6 \pm 9.13$	246.3/230
<b>GRB120524134*</b>	-0.128:0.128	Comp	$63.65 \pm 7.88$	$-0.2814 \pm 0.46$	-	259.40/228
	0.128:0.576	BB	-	-	$7.6 \pm 0.85$	258.60/229
	0.128:0.576	PL	-	$-2.28 \pm 0.29$	-	262.26/229
GRB120429003	-0.192:0.64	Comp	$576.6 \pm 503$	$-1.106 \pm 0.215$	-	292.8/227
	0.64:1.472	BB	-	-	$14.16 \pm 1.87$	224.80/228
GRB120327418	-0.192:-0.064	Comp	$309.7 \pm 268$	$-0.055 \pm 1.31$	-	260.64/223
	-0.064:0.064	BB	-	-	$38.45 \pm 7.99$	256.72/224
GRB120222021	-0.064:0.576	Comp	$139.1 \pm 95.62$	$-0.501 \pm 0.64$	-	243.02/253
	0.576:1.024	BB	-	-	$18.41 \pm 11.88$	324.71/254
GRB120101354	-0.096:0	Comp	$185.65 \pm 65.4$	$0.180 \pm 0.742$	-	214.57/222
	0:0.032	BB	-	-	$27.62 \pm 7.06$	176.82/223
GRB111207512	-0.896:-0.256	Comp	$730.11 \pm 817.50$	$-0.0781 \pm 1.07$	-	258.04/227
	-0.256:-0.128	BB	-	-	$1.624 \pm 0.43$	222.98/228
GRB111117510	-0.064:0.352	Comp	$519.6 \pm 222$	$-0.492 \pm 0$	-	280.64/224
	0.352:0.368	BB	-	-	$71.91 \pm 9.67$	210.20/225
GRB111011094	-0.064:0.128	Comp	$286.8 \pm 76.2$	$-0.379 \pm 0.261$	-	278.21/225
	0.128:1.408	BB	-	-	$11.53 \pm 6.31$	257.58/226
GRB111001804	-0.256:0	Comp	$504.3 \pm 490$	$-0.332 \pm 0.868$	-	256.90/223
	0:0.128	BB	-	-	$30.09 \pm 8.88$	205.96/224
GRB110605780	-0.256:0.768	Comp	$181.7 \pm 57.6$	$-0.105 \pm 0.69$	-	256.98/225
	0.768:1.28	BB	-	-	$20.223 \pm 6.99$	270.30/226
GRB110509475	-0.32:0.32	Comp	$403.8 \pm 284$	$-0.910 \pm 0.339$	-	236.66/233
	0.32:0.32	BB	-	-	$15.37 \pm 3.45$	255.28/224
GRB110227009	-0.192:0.640	Comp	$99.72 \pm 9.65$	$0.202 \pm 0.36$	-	216.43/221
	0.640:1.53	BB	-	-	$11.05 \pm 1.23$	231.45/222
GRB110131780	-0.192:0.064	Comp	$239.1 \pm 72.7$	$1.88 \pm 1.97$	-	239.12/216
	0.064:0.192	BB	-	-	$12.66 \pm 1.55$	215.15/217
GRB101216721	0.003:0.832	Comp	$108.5 \pm 29.64$	$-0.348 \pm 0.17$	-	272.27/253
	0.832:1.92	BB	-	-	$13.26 \pm 6.15$	394.2/254
<b>GRB101208498</b>	-0.64:0.64	Comp	$133.2 \pm 9.08$	$-0.941 \pm 0.067$	-	234.07/226
	0.64:1.408	BB	-	-	$7.847 \pm 2.07$	211.67/227
GRB101027230	-1.28:0.064	Comp	$409.8 \pm 121.6$	$1.78 \pm 0.73$	-	241.4/228
	0.064:0.064	BB	-	-	$29.14 \pm 7.12$	224.6/229
GRB100816026	0.003:1.408	Comp	$146.7 \pm 79.52$	$-0.244 \pm 0.19$	-	253.11/253
	1.408:2.048	BB	-	-	$24.71 \pm 9.1$	365.22/254
GRB100805300	-0.096:-0.032	Comp	$189 \pm 77.4$	$1.412 \pm 5.6$	-	142.99/128

Continued on next page...

Table 5 (continued)

GRB Names	Time (s)	Model	Epeak (keV)	Index	kT (keV)	C-stat/dof
	-0.032:-0.032	BB	-	-	52.62 $\pm$ 1.2	131.61/127
GRB100629801	-0.128-0.32	Comp	183.61 $\pm$ 25.7	-0.581 $\pm$ 0.198	-	246.6/224
	0.32-0.704	BB	-	-	31.14 $\pm$ 4	267.1/225
GRB100616773	-0.192:-0.064	Comp	472.8 $\pm$ 306	-0.341 $\pm$ 0.619	-	249.38/222
	-0.064:0	BB	-	-	54.59 $\pm$ 8.87	231.62/223
GRB100516396	-0.576:-0.064	Comp	200.1 $\pm$ 121.79	9.399 $\pm$ 0.597	-	278.46/253
	-0.064:0.064	BB	-	-	54.72 $\pm$ 29.13	232.6/254
GRB100417166	-0.048:-0.016	Comp	224.4 $\pm$ 60.8	-0.5763 $\pm$ 0.571	-	206.55/226
	-0.016:0.128	BB	-	-	48.11 $\pm$ 18.1	197.80/227
GRB100117879	-0.064:0.064	Comp	328.6 $\pm$ 132	-0.2533 $\pm$ 0.0	-	231.74/ 206
	0.064:0.192	BB	-	-	35.19 $\pm$ 6.11	226.37/227
GRB091126333	-0.064:0.064	Comp	177.1 $\pm$ 38.4	0.115 $\pm$ 0.586	-	257.52/ 230
	0.064:0.128	BB	-	-	38.81 $\pm$ 3.87	252.45/ 231
GRB091019750	-0.112:-0.016	Comp	696 $\pm$ 636	-0.402 $\pm$ 0.609	-	243.50/217
	-0.016:0.096	BB	-	-	73.32 $\pm$ 19.5	203.47/218
GRB091019750	-0.112:-0.016	Comp	388.5 $\pm$ 161	-0.6045 $\pm$ 2.33	-	264.2/225
	-0.016:0.096	BB	-	-	16.11 $\pm$ 2.33	228.16/226
GRB091006360	-0.192:-0.064	Comp	193.1 $\pm$ 79.61	-0.508 $\pm$ 0.23	-	222.5/253
	-0.064:0	BB	-	-	67.68 $\pm$ 45.63	247.95/254
GRB090927422	-0.192:0.192	Comp	106.7 $\pm$ 19.2	0.460 $\pm$ 0.07	-	256.15/226
	0.192:0.32	BB	-	-	25.91 $\pm$ 6.15	209.32/227
<b>GRB090616157</b>	-0.192:0.512	Comp	1576 $\pm$ 709	-1.370 $\pm$ 0.27	-	206.75/229
	0.512:0.96	BB	-	-	52.98 $\pm$ 35.8	269.58/230
<b>GRB090518080</b>	-0.64:768	Comp	286.0 $\pm$ 163	-1.235 $\pm$ 0.18	-	224.53/229
	0.768:1.408	BB	-	-	28.83 $\pm$ 4.46	217.93/230
<b>GRB090108020*</b>	-0.064:0.256	Comp	140.3 $\pm$ 87.35	-0.424 $\pm$ 0.19	-	226.05/223
	0.256:0.64	BB	-	-	10.73 $\pm$ 6.93	242.93/224
	0.256:0.64	PL	-	-1.87 $\pm$ 0.13	-	238.29/224
GRB081230871	-0.128:0.192	Comp	320.60 $\pm$ 96.1	2.050 $\pm$ 1.90	-	234.01/226
	0.192:0.384	BB	-	-	92.35 $\pm$ 17.3	226.28/ 227
GRB081226044	-0.192:0.192	Comp	532.7 $\pm$ 417	-0.959 $\pm$ 0.271	-	207.44/ 222
	0.192:0.64	BB	-	-	38.29 $\pm$ 4.86	208.99/223
GRB081223419	-0.064:0.256	Comp	197 $\pm$ 30.5	-0.429 $\pm$ 0.21	-	230/226
	0.256:0.512	BB	-	-	23.78 $\pm$ 2.6	259.8/227
<b>GRB081122614*</b>	-0.128:0.192	Comp	143.8 $\pm$ 22.0	-1.331 $\pm$ 0.39	-	193.67/221
	0.192:0.832	BB	-	-	11.26 $\pm$ 6.98	193.52 /222
	0.192:0.832	PL	-	-1.93 $\pm$ 1.71	-	194.03/222
<b>GRB081107321</b>	-0.192:1.152	Comp	72.73 $\pm$ 38.19	-0.3865 $\pm$ 0.097	-	317.48/253
	1.152:1.472	BB	-	-	17.17 $\pm$ 9.85	285.96/254
GRB081101491	-0.064-0.064	Comp	551.8 $\pm$ 437.1	0.835 $\pm$ 0.331	-	238.6/226
	0.064-0.06	BB	-	-	37.6 $\pm$ 9.69	241.4/227
GRB080919790	-0.128:0.064	Comp	183.6 $\pm$ 116.7	-0.2307 $\pm$ 0.072	-	232.48/253
	0.064:0.384	BB	-	-	37.23 $\pm$ 9.66	283.91/254
GRB080831053	-0.288:0	Comp	154 $\pm$ 41.2	1.305 $\pm$ 1.89	-	207.31/ 230
	0:0.288	BB	-	-	41.92 $\pm$ 10.4	221.39/231

This paper has been typeset from a  $\text{\LaTeX}$  file prepared by the author.